

NANOMATERIALS

Coherent, atomically thin transition-metal dichalcogenide superlattices with engineered strain

Saien Xie,^{1,2} Lijie Tu,^{1*} Yimo Han,^{1*} Lujie Huang,³ Kibum Kang,² Ka Un Lao,³ Preeti Poddar,² Chibeom Park,² David A. Muller,^{1,4} Robert A. DiStasio Jr.,³ Jiwoong Park^{2,3,†}

Epitaxy forms the basis of modern electronics and optoelectronics. We report coherent atomically thin superlattices in which different transition metal dichalcogenide monolayers—despite large lattice mismatches—are repeated and laterally integrated without dislocations within the monolayer plane. Grown by an omnidirectional epitaxy, these superlattices display fully matched lattice constants across heterointerfaces while maintaining an isotropic lattice structure and triangular symmetry. This strong epitaxial strain is precisely engineered via the nanoscale supercell dimensions, thereby enabling broad tuning of the optical properties and producing photoluminescence peak shifts as large as 250 millielectron volts. We present theoretical models to explain this coherent growth and the energetic interplay governing the ripple formation in these strained monolayers. Such coherent superlattices provide building blocks with targeted functionalities at the atomically thin limit.

Epitaxial structures with coherent heterointerfaces, in which lattices of dissimilar materials are matched without dislocations, enable advanced scientific and technological applications, including multiferroic oxides with engineered strain and symmetry (1, 2), high-performance quantum cascade lasers (3), and high-efficiency light-emitting diodes (4). Two-dimensional (2D) coherent heterostructures and superlattices (Fig. 1, A and B) can serve as ultrathin building blocks for advanced stacking and hetero-integration with other materials (5–7) and provide opportunities not available with their 3D analogs. Realizing this goal would require the integration of various 2D materials whose properties can be tuned by the strain required for coherent lattice matching, as well as a method for precisely controlling the superlattice dimensions while maintaining lattice coherence over the entire structure. Monolayer transition metal dichalcogenides (TMDs), many of which share similar crystal structures, provide an ideal material platform with diverse electrical, optical (8, 9), piezoelectric (10, 11), and valley properties (12). However, recent studies on TMD heterostructure synthesis have shown only limited capabilities toward realizing coherent 2D superlattices (13–21).

We report coherent monolayer TMD superlattices with precisely controlled supercell dimensions and lattice coherence maintained over the entire structure, which result in broad tuning

of their optical properties. We used WS₂ and WSe₂ as the two main TMDs for our heterostructures and superlattices (Fig. 1A, inset), where the repeat direction of the superlattice is in the growth plane of a monolayer, rather than the out-of-plane direction of conventional thin-film superlattices. These TMDs have a substantial lattice mismatch (Δ) of $\sim 4\%$, with WSe₂ having

the larger lattice constant. In scanning electron microscope (SEM) images of three representative WS₂/WSe₂ heterostructures with controlled supercell dimensions (Fig. 1C), dark (bright) regions correspond to WS₂ (WSe₂) monolayers. Every triangular unit of WS₂ and WSe₂ shows a highly symmetric, equilateral triangular shape of uniform width, each defined by straight, parallel heterointerfaces, that could be directly controlled with nanoscale precision. These widths could be as narrow as 20 nm (Fig. 1C, center) and periodically modulated to form superlattices with different dimensions, represented by the two widths $\{d_{\text{WS}_2}$ and $d_{\text{WSe}_2}\}$. Two examples of superlattices are shown, one primarily composed of WS₂ ($d_{\text{WS}_2} \gg d_{\text{WSe}_2}$) (Fig. 1C, left) and the other by WSe₂ ($d_{\text{WS}_2} \ll d_{\text{WSe}_2}$) (Fig. 1C, right). Heterostructures consisting of different metal and chalcogen elements could also be synthesized with a similar level of control (see fig. S1C for an example of a WSe₂/MoS₂/WS₂ heterostructure).

These crystalline TMD superlattices were synthesized by a modulated metal-organic chemical vapor deposition (MOCVD) (22) process (see Fig. 1, supplementary materials, and fig. S1), with two distinctive features compared with previous approaches (13–21). First, the concentration of each precursor was individually and precisely controlled, which allowed the direct tuning of the supercell dimensions. The composition of TMD could be switched, for example, from WS₂ to WSe₂ and vice versa, by simply changing the chalcogen precursors. The width of each component was determined by controlling the timing of the switch, according

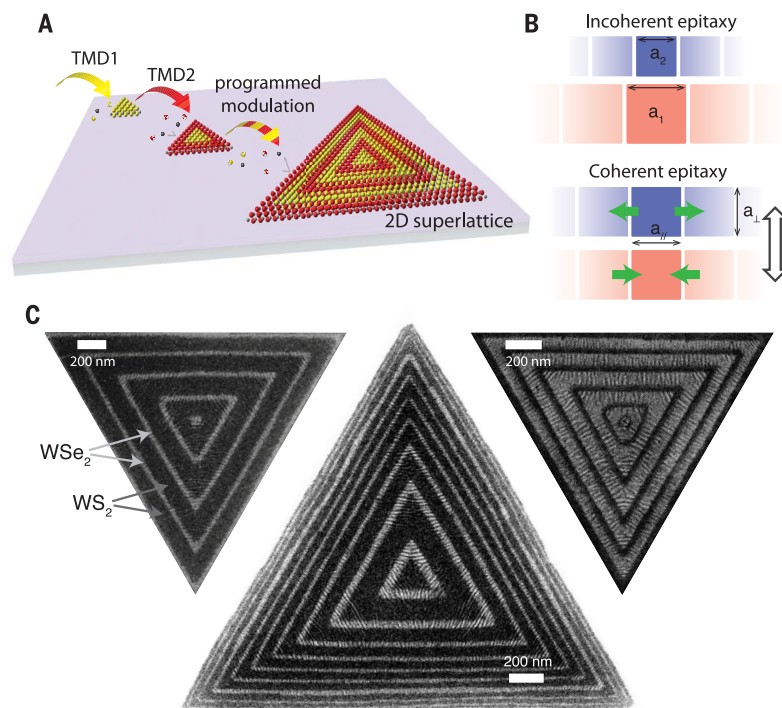


Fig. 1. 2D monolayer TMD superlattices. (A) Schematic of 2D superlattices based on monolayer TMDs. (B) Schematic of incoherent and coherent epitaxy, with the epitaxy direction represented by the outlined arrow. (C) SEM images of three monolayer WS₂/WSe₂ superlattices. Scale bars, 200 nm.

¹School of Applied and Engineering Physics, Cornell University, Ithaca, NY 14853, USA. ²Department of Chemistry, Institute for Molecular Engineering, and James Franck Institute, University of Chicago, Chicago, IL 60637, USA. ³Department of Chemistry and Chemical Biology, Cornell University, Ithaca, NY 14853, USA. ⁴Kavli Institute at Cornell for Nanoscale Science, Cornell University, Ithaca, NY 14853, USA.

*These authors contributed equally to this work.

†Corresponding author. Email: jwpark@uchicago.edu

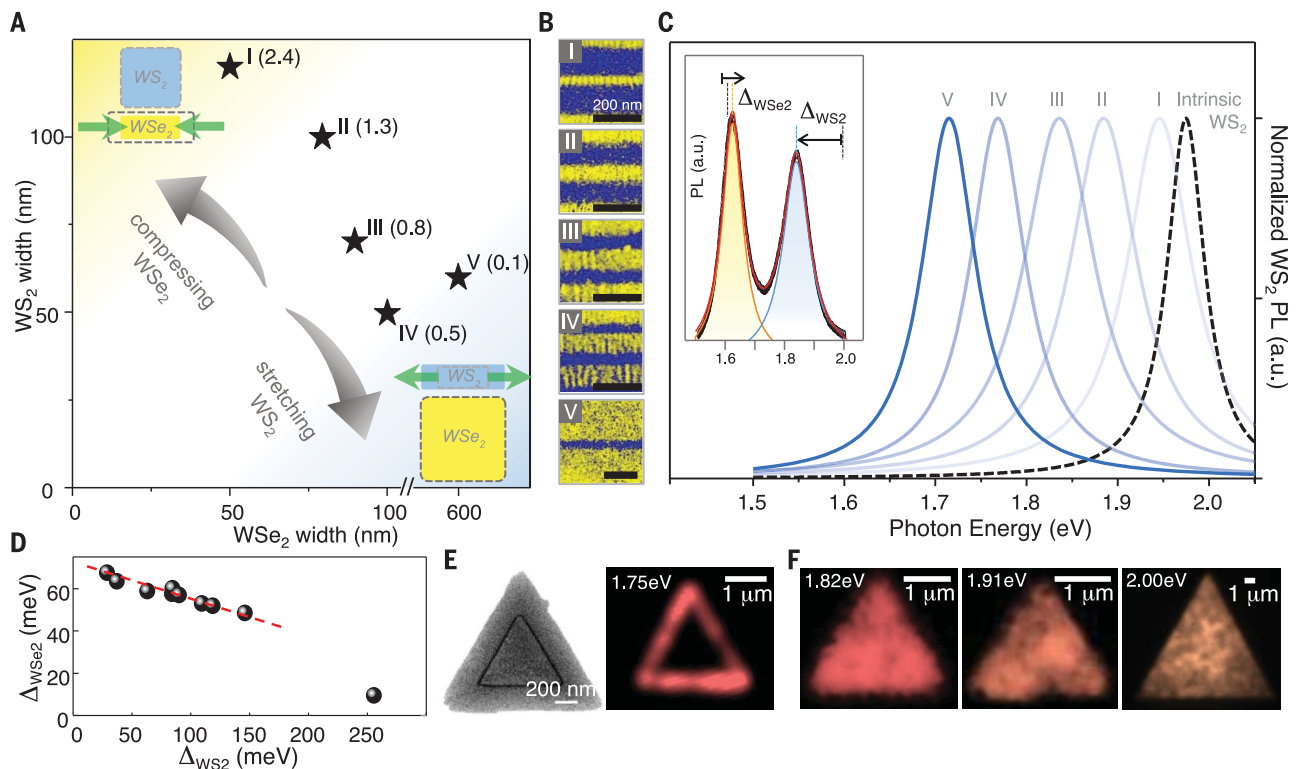


Fig. 3. Strain engineering of PL of WS₂/WSe₂ superlattices. (A) Plot of WS₂/WSe₂ superlattices I to V with different ratios $\rho = d_{\text{WS}_2}/d_{\text{WSe}_2}$ (values shown in parentheses). (Insets) Schematic of supercell dimension-dependent strain magnitude in the superlattice. (B) False-color SEM images of superlattices I to V. Scale bars, 200 nm. (C) Normalized PL spectra of WS₂ for intrinsic WS₂ (dashed line) and superlattices I to V. (Inset) A representative PL spectrum of a WS₂/WSe₂ superlattice showing the WS₂ peak red-shifted by

Δ_{WSe_2} and the WSe₂ peak blue-shifted by Δ_{WS_2} . (D) Plot of $\Delta_{\text{WSe}_2} - \Delta_{\text{WS}_2}$ for WS₂/WSe₂ superlattices with different supercell dimensions. (E) (Left) SEM image of a narrow WS₂ stripe embedded in WSe₂. (Right) PL image of a heterostructure similar to the left, taken at photon energy of 1.75 eV. (F) PL images of two WS₂/WSe₂ superlattices at photon energies near their WS₂ peak positions (left and middle, at 1.82 eV and 1.91 eV, respectively) and an intrinsic monolayer WS₂ (right, at 2.00 eV). Scale bars, 1 μm .

from another superlattice {75 and 60 nm}, each plotting a_{\parallel} , a_{\perp} , and lattice rotation. The superlattice consists of three regions (α , β , and γ , as outlined in Fig. 2F), with heterointerface orientations rotated by 120° from each other. The orientations of a_{\parallel} and a_{\perp} are different for α , β , and γ and are defined relative to the heterointerfaces in each region. The a_{\parallel} map (Fig. 2F, left) showed little contrast between WS₂ and WSe₂, generating a single histogram peak as shown in Fig. 2H, left (region α ; see fig. S4 for β and γ histograms). The a_{\perp} map showed a small contrast between the WS₂ and WSe₂ regions, generating two peaks (Fig. 2H, left) centered 0.4% below (corresponding to WS₂) and 0.8% above (corresponding to WSe₂) the a_{\parallel} peak, resulting in $\delta_{\perp} = 1.2\%$, as seen in Fig. 2D. Third, the lattice rotation map resolved only one dislocation clearly (arrow) within the entire superlattice (lateral size $\sim 3.2 \mu\text{m}$), suggesting the existence of a dislocation-free, coherent lattice everywhere, including the boundary regions between the α , β , and γ regions. In contrast, incoherent heterostructures showed arrays of dislocations at heterointerfaces (fig. S5).

Figure 2 shows that $\delta_{\parallel} = 0$ everywhere, confirming coherent heterointerfaces in our superlattice. In addition, the lattice isotropy and rotational symmetry were maintained over the entire superlattice. Our TEM and EMPAD data

confirm (i) nearly identical and isotropic unit cell dimensions for both the WS₂ and WSe₂ regions; (ii) that the lattice orientation in our EMPAD map (Fig. 2G) was highly uniform (standard deviation $< 1 \text{ mrad}$), consistent with the observed sharp and isotropic TEM diffraction spots (Fig. 2, C and D); and (iii) that the superlattice is triangular with straight edges and heterointerfaces. This result is in sharp contrast to the lattice anisotropy expected from conventional unidirectional epitaxy, where a_{\parallel} is matched for the epilayers and a_{\perp} is free from any constraints, causing the superlattice to have a different symmetry from that of the original crystal. Instead, our superlattice grew with coherent omnidirectional epitaxy (see supplementary text and fig. S6), where regions of different epitaxy directions (α , β , and γ) coherently connect with each other while maintaining the same symmetry of the original crystal.

The perfect symmetry in our coherent superlattices imposes an additional constraint that requires identical values of a_{\perp} for both WS₂ and WSe₂. This feature is further illustrated in Fig. 2I: When a triangular WSe₂ unit was replaced by WS₂, the latter needed to expand by the same amount in all directions (i.e., larger a_{\parallel} and a_{\perp}) to coherently bridge the inner and outer triangular WSe₂ units. This ideal picture changes in real

superlattices with finite bulk and shear moduli values, where the final structure will minimize the total elastic strain energy. In this case, the lattice would deviate from having identical a_{\perp} values for WS₂ and WSe₂, resulting in $0 \leq \delta_{\perp} < \Delta$, as seen from our data.

These observations were quantitatively predicted by coarse-grained simulations of these superlattices that account for both bond and angle interactions on an appropriate footing (Fig. 2H, right, and 2J). In this regard, it is the inclusion of angular interactions, in particular, that accounts for the shear stiffness inside the TMD superlattice and thereby introduces local frustration (analogous to the antiferromagnetic triangular-lattice Ising model) that is key to predicting coherent omnidirectional epitaxy across the entire lattice, as well as a small but nonvanishing δ_{\perp} (see fig. S7 and supplementary materials). The lattice coherence further allows for high-performance p-n diodes showing high rectification ratios ($> 10^6$) and electroluminescence, as well as double heterostructure transistors, which we successfully fabricated using our heterostructures (see figs. S8 and S9 and supplementary text).

This lattice coherence also resulted in a tensile (compressive) strain within the WS₂ (WSe₂) region in our superlattices, the magnitude of which varied depending on the supercell dimensions.

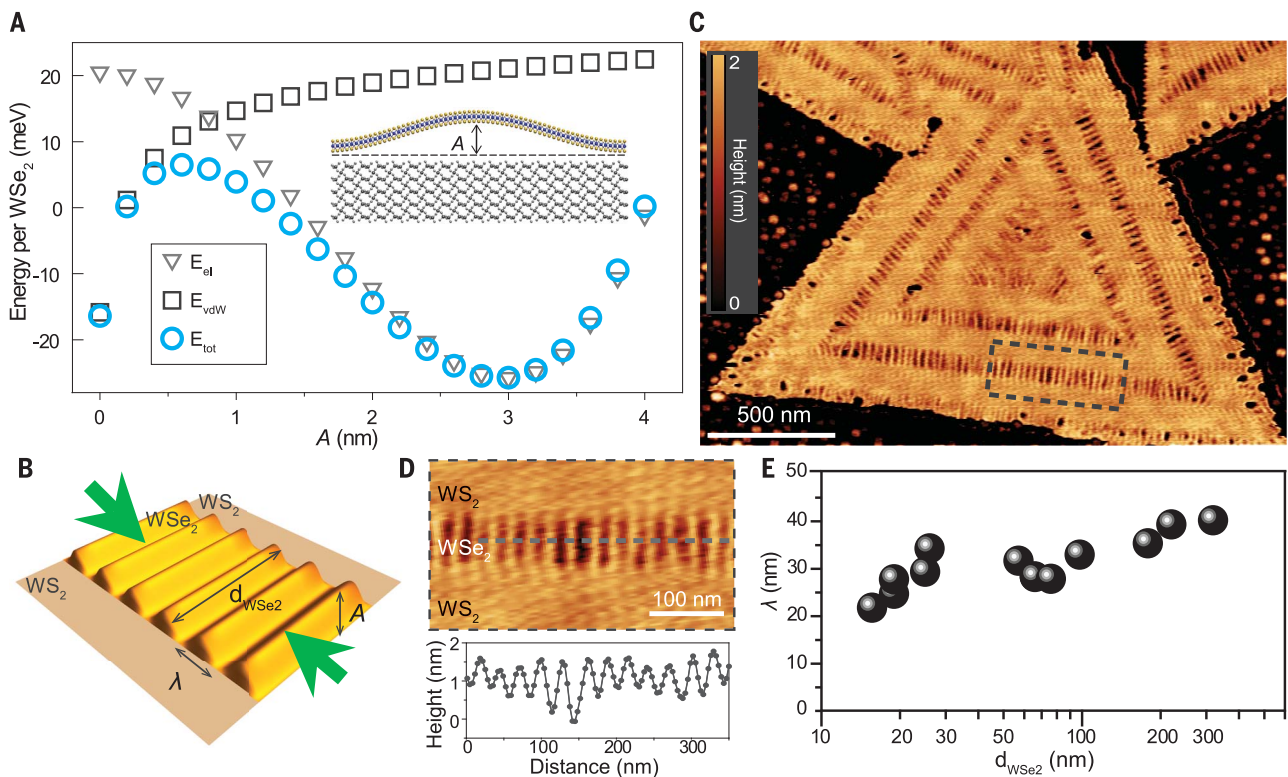


Fig. 4. Formation of out-of-plane ripples in WSe₂. (A) Theoretically calculated elastic strain energy (E_{el}), interlayer van der Waals binding energy (E_{vdW}), and total energy (E_{tot}) per WSe₂ as a function of WSe₂ ripple height (A) (E_{el} and E_{vdW} shifted by -32 meV and 53 meV, respectively, for clarity). (Inset) Schematic of the rippled WSe₂ on substrate. (B) Schematic

of rippled WSe₂ and flat WS₂, where the ripple wavelength (λ), A , and d_{WSe_2} are indicated. (C) AFM height image of a representative WS₂/WSe₂ superlattice. Scale bar, 500 nm. (D) Enlarged AFM image of the boxed area in (C) and height profile along the dashed line. Scale bar, 100 nm. (E) λ of superlattices with different d_{WSe_2} .

Figure 3A illustrates such strain control. For example, a smaller d_{WS_2} or larger d_{WSe_2} (with a small ratio $\rho = d_{WS_2}/d_{WSe_2}$) increased the tensile strain in WS₂ and decreased the compressive strain in WSe₂, as it brought $a_{//}$ and a_{\perp} closer to the intrinsic values for WSe₂. In addition, the band structure of both WS₂ and WSe₂ was sensitive to the applied strain; the size of the direct band gap decreased (increased) when subjected to tensile (compressive) strain (26–29).

This strain-dependent band structure allowed for broad tuning of the optical properties by superlattice design. Figure 3B shows the false-color SEM images of five representative WS₂ (blue)/WSe₂ (yellow) coherent superlattices I to V with different ρ (dimensions plotted in Fig. 3A). The resulting photoluminescence (PL) spectra showed two peaks, with one corresponding to WS₂ and the other to WSe₂ (Fig. 3C, inset). However, the WS₂ peak was red-shifted from the intrinsic peak energy of 1.97 eV by Δ_{WS_2} , whereas the WSe₂ peak was blue-shifted from the intrinsic value of 1.61 eV by Δ_{WSe_2} . Figure 3C compares the normalized WS₂ peaks measured from superlattices I to V (each extracted from the full PL spectra) to the intrinsic WS₂ peak (dashed curve). Superlattices with smaller ρ showed larger Δ_{WS_2} , as large as 250 meV (see Fig. S10 for representative original PL spectra). Figure 3D further plots Δ_{WS_2} versus Δ_{WSe_2} for additional superlattices with different supercell dimensions.

These PL characteristics were consistent with the strain engineered by the superlattice design. The positive values for both Δ_{WS_2} and Δ_{WSe_2} confirmed the tensile (compressive) strain in WS₂ (WSe₂). Their magnitudes showed a negative correlation, which is consistent with their expected negatively correlated strain magnitude (Fig. 3A). The largest Δ_{WS_2} of 250 meV, corresponding to a 3.4% uniaxial strain or a 1.4% isotropic biaxial strain (26), was consistent with the large tensile strain expected from superlattice V with a small $\rho = 0.1$. Moreover, the PL image (Fig. 3E, right; taken at 1.75 eV) confirmed that the highly red-shifted WS₂ PL peak indeed originated from the strained WS₂ region (SEM image of a similarly grown sample shown in Fig. 3E, left). In general, superlattices with supercell dimensions below the diffraction limit (Fig. 3F, left and middle) showed uniform PL intensities at their respective peak energies over the entire structure, with a similar uniformity compared with intrinsic WS₂ (Fig. 3F, right).

Strained thin films relax through out-of-plane deformations such as wrinkles and ripples, which makes these films nonflat and their edges curved (30–32). However, our ultrathin superlattices maintained lattice coherence and symmetry, despite being highly strained and their edges being under alternating compressive and tensile stress during growth, because of strong van der Waals (vdW) interactions between the super-

lattice and the underlying growth substrate (5, 33) (SiO₂ in our experiment), which keep the 2D superlattice flat. Figure 4A plots the theoretically calculated total energy (E_{tot} , circles) per WSe₂ of a strained WSe₂ monolayer on SiO₂ as a function of the out-of-plane ripple height (A , measured from peak to valley; see schematic in Fig. 4B). E_{tot} consists of the elastic strain energy (E_{el} , triangles), computed using a macroscopic elastic energy model (that accounts for both stretching and bending energy components in an ultrathin film), and the interlayer vdW binding energy between the WSe₂ and SiO₂ (E_{vdW} , squares), computed using an all-atom quantum-mechanical vdW energy model (see supplementary text and fig. S11). Although the rippled state ($A \approx 3$ nm) that relaxes the compressive strain is lowest in energy, the energetic profile shows another minimum at $A = 0$ nm, corresponding to the flat state. These two states have similar energies because the reduction in E_{el} roughly equals the increase in E_{vdW} for the rippled state.

The rippled and flat states are separated by an energetic barrier (with an activation energy of 10 to 20 meV per WSe₂), because the increase in A in the regime $0 < A < 1$ nm rapidly destabilizes E_{vdW} without substantially stabilizing E_{el} . Figure 4A thus predicts that the attractive vdW force from the substrate keeps WSe₂ flat and that the transition from the flat to rippled state can only occur in the presence of a substantial perturbation.

As a result, these theoretical findings suggest that the synthesis conditions in our experiment, which maintained a constant growth environment with no strong perturbations, allowed the superlattice to remain flat and the growth edge straight during growth.

The superlattices reported here were subjected to a cool-down process after growth, from a relatively high growth temperature (600°C) to room temperature. This process could perturb the samples (e.g., thermal expansion/contraction of the superlattice and SiO₂) and induce ripples in WSe₂, which is what we observed in our samples. The atomic force microscope (AFM) height image of a representative WS₂/WSe₂ superlattice (Fig. 4C) shows out-of-plane ripples in WSe₂ (schematically illustrated in Fig. 4B). These ripples ran continuously across the WSe₂ stripes only and were periodic along the heterointerfaces, as shown in the enlarged AFM image (Fig. 4D, top). The peak-to-valley height (A) was between 1 and 2 nm (measured from the AFM profile shown in Fig. 4D, bottom). This value is surprisingly near that of A for the lowest energy state in Fig. 4A, despite the use of a simple energetic model and an idealized superlattice geometry. We also observed that the ripple wavelengths (λ) for superlattices with different d_{WSe_2} remained relatively constant (near 30 nm, as shown in Fig. 4E), with little dependence on d_{WSe_2} over one order of magnitude (ranging from 20 to 320 nm). This result suggests that the presence of WS₂/WSe₂ interfaces had minimal effect on the energetics of the ripple formation in this regime and that the constant compressive strain in WSe₂ (even up to $d_{\text{WSe}_2} = 320$ nm) was released through rippling. This finding also explains the smaller range of Δ_{WSe_2} shown in Fig. 3D.

For superlattices with $d_{\text{WSe}_2} > 320$ nm, however, the periodic ripples were no longer continuous across the WSe₂ area (see fig. S12). This difference indicates the presence of an alternative strain relaxation mechanism, including the formation of misfit dislocations and a coherence length of ~320 nm for our WS₂/WSe₂ superlattices. This coherence length was substantially greater than the critical thickness of 2 nm for the Si/Ge system with a similar $\Delta \sim 4\%$ (34), as well as the critical thickness for the WS₂/WSe₂ system estimated using the People-Bean model (below 20 nm) (see supplementary materials and fig. S13)

(35). A full explanation for such a long coherence length would require a general theory optimized for 2D, which is currently lacking. However, we expect that our stable superlattice growth conditions and a larger energetic barrier for dislocation formation in 2D systems may account for the long coherence length. For example, there are limited configurations of covalent bonding for dislocations in 2D systems and no screw dislocations. Our demonstration of omnidirectional coherent 2D superlattices not only presents a powerful framework for the epitaxial synthesis of nanomaterials and the engineering of their properties but also opens up the possibility of a new interdisciplinary research direction because our coherent superlattice is crystalline yet highly deformable. Generation of ordered arrays of coherent superlattices would further accelerate their electronic and optoelectronic applications, which may be achieved with improved spatial control of nucleation (36) and superlattice orientation (37, 38).

REFERENCES AND NOTES

1. J. Wang *et al.*, *Science* **299**, 1719–1722 (2003).
2. D. G. Schlom *et al.*, *MRS Bull.* **39**, 118–130 (2014).
3. J. Faist *et al.*, *Science* **264**, 553–556 (1994).
4. S. Nakamura, *Science* **281**, 955–961 (1998).
5. A. K. Geim, I. V. Grigorieva, *Nature* **499**, 419–425 (2013).
6. D. Jariwala, T. J. Marks, M. C. Hersam, *Nat. Mater.* **16**, 170–181 (2017).
7. D. Sarkar *et al.*, *Nature* **526**, 91–95 (2015).
8. Q. H. Wang, K. Kalantar-Zadeh, A. Kis, J. N. Coleman, M. S. Strano, *Nat. Nanotechnol.* **7**, 699–712 (2012).
9. X. Xu, W. Yao, D. Xiao, T. F. Heinz, *Nat. Phys.* **10**, 343–350 (2014).
10. W. Wu *et al.*, *Nature* **514**, 470–474 (2014).
11. H. Zhu *et al.*, *Nat. Nanotechnol.* **10**, 151–155 (2015).
12. K. F. Mak, J. Shan, *Nat. Photonics* **10**, 216–226 (2016).
13. X. Duan *et al.*, *Nat. Nanotechnol.* **9**, 1024–1030 (2014).
14. Y. Gong *et al.*, *Nat. Mater.* **13**, 1135–1142 (2014).
15. C. Huang *et al.*, *Nat. Mater.* **13**, 1096–1101 (2014).
16. M.-Y. Li *et al.*, *Science* **349**, 524–528 (2015).
17. K. Chen *et al.*, *ACS Nano* **9**, 9868–9876 (2015).
18. Y. Gong *et al.*, *Nano Lett.* **15**, 6135–6141 (2015).
19. X. Q. Zhang, C. H. Lin, Y. W. Tseng, K. H. Huang, Y. H. Lee, *Nano Lett.* **15**, 410–415 (2015).
20. H. Heo *et al.*, *Adv. Mater.* **27**, 3803–3810 (2015).
21. K. Bogaert *et al.*, *Nano Lett.* **16**, 5129–5134 (2016).
22. K. Kang *et al.*, *Nature* **520**, 656–660 (2015).
23. S. Helveg *et al.*, *Phys. Rev. Lett.* **84**, 951–954 (2000).
24. J. V. Lauritsen *et al.*, *Nat. Nanotechnol.* **2**, 53–58 (2007).
25. M. W. Tate *et al.*, *Microsc. Microanal.* **22**, 237–249 (2016).
26. P. Johari, V. B. Shenoy, *ACS Nano* **6**, 5449–5456 (2012).
27. Y. Wang *et al.*, *Nano Res.* **8**, 2562–2572 (2015).
28. R. Schmidt *et al.*, *2D Mater.* **3**, 021011 (2016).
29. R. Frisenda *et al.*, *npj 2D Mater. Appl.* **1**, 10 (2017).

30. Y. Klein, E. Efrati, E. Sharon, *Science* **315**, 1116–1120 (2007).
31. B. Davidovitch, R. D. Schroll, D. Vella, M. Adda-Bedia, E. A. Cerda, *Proc. Natl. Acad. Sci. U.S.A.* **108**, 18227–18232 (2011).
32. D. Nandwana, E. Ertekin, *Nano Lett.* **15**, 1468–1475 (2015).
33. A. Ambrosetti, N. Ferri, R. A. DiStasio Jr., A. Tkatchenko, *Science* **351**, 1171–1176 (2016).
34. J. W. Matthews, A. E. Blakeslee, *J. Cryst. Growth* **27**, 118–125 (1974).
35. R. People, J. C. Bean, *Appl. Phys. Lett.* **47**, 322–324 (1985).
36. S. Najmaei *et al.*, *Nat. Mater.* **12**, 754–759 (2013).
37. D. Dumcenco *et al.*, *ACS Nano* **9**, 4611–4620 (2015).
38. D. Ruzmetov *et al.*, *ACS Nano* **10**, 3580–3588 (2016).

ACKNOWLEDGMENTS

We thank S. Nagel, T. Witten, and A. Tkatchenko for helpful discussions. We thank J.-U. Lee for help with EL measurements. **Funding:** This work was primarily supported by the Air Force Office of Scientific Research (FA9550-16-1-0031, FA9550-16-1-0347, and FA2386-13-1-4118) and the National Science Foundation (NSF) through the Cornell Center for Materials Research with funding from the NSF Materials Research Science and Engineering Centers (MRSEC) program (DMR-1719875), the University of Chicago MRSEC (NSF DMR-1420709), and the Platform for the Accelerated Realization, Analysis, and Discovery of Interface Materials (PARADIM; DMR-1539918). Additional funding was provided by the Samsung Advanced Institute of Technology. Material characterizations including electron microscopy were supported by the Cornell Center for Materials Research (NSF DMR-1719875) and the MRSEC Shared User Facilities at the University of Chicago (NSF DMR-1420709). L.T., K.U.L., and R.D. acknowledge partial support from Cornell University through start-up funding. This research used resources of the Argonne Leadership Computing Facility at Argonne National Laboratory, which is supported by the Office of Science of the U.S. Department of Energy under contract no. DE-AC02-06CH11357 and resources of the National Energy Research Scientific Computing Center, which is supported by the Office of Science of the U.S. Department of Energy under contract no. DE-AC02-05CH11231. **Author contributions:** S.X. and J.P. conceived the experiments. S.X. developed the superlattice synthesis and performed DF-TEM, electron diffraction, and optical measurements. Y.H. and D.A.M. conducted the atomic-resolution STEM imaging and EMPAD characterizations. L.T., K.U.L., and R.A.D. developed and conducted the coarse-grained simulations and vdW calculations. S.X., K.K., and C.P. carried out AFM and SEM characterizations, and S.X., L.H., and P.P. performed the device fabrication and measurements. S.X., R.A.D., and J.P. wrote the manuscript. All authors discussed and commented on the manuscript. **Competing interests:** The authors declare no competing financial interests. A provisional U.S. patent has been filed based on this work. **Data and materials availability:** All data are reported in the main text and supplementary materials.

SUPPLEMENTARY MATERIALS

www.sciencemag.org/content/359/6380/1131/suppl/DC1
Materials and Methods
Supplementary Text
Figs. S1 to S13
Table S1
References (39–61)

9 August 2017; accepted 22 January 2018
10.1126/science.aao5360

Coherent, atomically thin transition-metal dichalcogenide superlattices with engineered strain

Saien Xie, Lijie Tu, Yimo Han, Lujie Huang, Kibum Kang, Ka Un Lao, Preeti Poddar, Chibeom Park, David A. Muller, Robert A. DiStasio Jr. and Jiwoong Park

Science **359** (6380), 1131-1136.
DOI: 10.1126/science.aao5360

Coherent strained superlattices

Two-dimensional superlattices represent the atomic-thickness limit of heterostructures that enable technologies such as strain-engineered multiferroics and quantum-cascade lasers. Xie *et al.* were able to produce monolayer superlattices of transition metal dichalcogenides (WS_2 and WSe_2) with full lattice coherence, despite a 4% lattice mismatch. They used a modulated metal-organic chemical vapor deposition process that precisely controlled each precursor. Furthermore, the authors could strain-engineer the optical properties of the superlattices to observe out-of-plane rippling.

Science, this issue p. 1131

ARTICLE TOOLS

<http://science.sciencemag.org/content/359/6380/1131>

SUPPLEMENTARY MATERIALS

<http://science.sciencemag.org/content/suppl/2018/03/07/359.6380.1131.DC1>

REFERENCES

This article cites 58 articles, 8 of which you can access for free
<http://science.sciencemag.org/content/359/6380/1131#BIBL>

PERMISSIONS

<http://www.sciencemag.org/help/reprints-and-permissions>

Use of this article is subject to the [Terms of Service](#)